Geomorphology 470 (2025) 109545

Contents lists available at ScienceDirect

Geomorphology

journal homepage: www.journals.elsevier.com/geomorphology

Evolution of deep-seated gravitational slope deformation in a deep valley of the Czech Flysch Carpathians

Vladimír Chalupa [a], Tomáš Pánek [a], Michal Břežný [a], Francisco Gutiérrez [b,*], Alicia Medialdea [c]

[a] Department of Physical Geography and Geoecology, Faculty of Science, University of Ostrava, Chittussiho 10, Ostrava 710 00, Czech Republic
[b] Department of Earth Sciences, University of Zaragoza, Zaragoza, Spain
[c] Centro Nacional de Investigación sobre la Evolución Humana (CENIEH), Burgos, Spain

ARTICLE INFO

Keywords:
Deep-seated gravitational deformation
Trenching
Dating
Geophysics
Flysch Carpathians

ABSTRACT

In the Czech Outer Western Carpathians (OWC), the lower limit of deep-seated gravitational slope deformations (DSGSDs) occur associated with moderate local relief and slope gradient, showing a limited degree of geomorphic development. Here, DSGSDs display a relatively high spatial frequency, despite the limited tectonic and seismic activity, often claimed as major preparatory and triggering factors. Nonetheless, favourable stratigraphic and structural features in flysch successions, together with fluvial downcutting, provide conditions prone to DSGSDs. The study area of Travný Mt. hosts the typical DSGSDs in the highest part of Czech OWC. With the aim of unravelling the controlling and triggering factors, the internal structure, and the timing and kinematics of mass-movement activity, a multidisciplinary investigation was performed. LiDAR-based and field geomorphological mapping allowed to constrain the extent of the of DSGSD, expressed by characteristic landforms such as antislope scarps and grabens. The structural analysis and geophysical surveys (ERT and GPR) provided insight into the internal structure of the DSGSD, reaching a depth of >100 m, and supported its mountain-scale spatial propagation. The instability is controlled by inherited faults, deep-penetrating joints and and the stratigraphic contact between brittle caprock overlying weaker rocks. Morphologically, the most prominent deformation is located in the upper part, which is dominated by toppling of flysch blocks with thick-bedded sandstone. The results of the trenching technique and geochronological analyses point to the episodic kinematics of this portion of the DSGSD, revealing a significant displacement event (ca. 9.9 ka) linked to a major climate change occurred after the Late Glacial/Holocene transition.

1. Introduction

This work illustrates the characterization of a deep-seated gravitational slope deformations (DSGSDs) and the reconstruction of its evolution integrating data gathered by multiple techniques. DSGSDs have been recognized as worldwide phenomena (Agliardi et al., 2009a, 2009b; Pánek et al., 2011; Crosta et al., 2013; Lebourg et al., 2014; Břežný et al., 2018a; Pánek et al., 2019; Di Luzio et al., 2022), although there is often significant uncertainty regarding the stress-strain mechanisms involved in their development (Lo Russo et al., 2012). Usually, DSGSDs occur on high-relief and steep slopes of mountain regions (Crosta et al., 2013; Teshebaeva et al., 2019; García-Delgado, 2020) and have been ascribed to a wide variety of deformational mechanisms: rock creep (Nemčok, 1982; Crosta et al., 2013), gravitational faulting (Gutiérrez-Santolalla et al., 2005; Gutiérrez et al., 2008; McCalpin and Jones, 2021), sagging/sackung (Agliardi et al., 2001; Jomard et al., 2014), toppling (Bovis, 1982; Glueer et al., 2019; McCalpin and Corominas, 2019), interstratal evaporite dissolution (Guglielmi et al., 2000; Alberto et al., 2008; Jaboyedoff et al., 2011), or salt flow (McGill and Stromquist, 1979; Gutiérrez et al., 2012). DSGSDs are typically expressed in the landscape by surface-deformation landforms such as double/multiple ridges and ridge-top depressions, scarps, antislope scarps (also designated as counterscarps or uphill-facing scarps), graben depressions and internally drained troughs, ground fissures and associated ravelling sinkholes, rotated blocks, and toe bulging (Agliardi et al., 2001; Jaboyedoff et al., 2011; Pánek et al., 2011; Crosta et al., 2013; Chalupa et al., 2021). Well-developed DSGSDs in high-mountain regions often show combinations of several such landforms (Agliardi et al., 2001). Commonly invoked predisposing, preparatory and triggering factors include favourable litho-structural conditions associated with

* Corresponding author.
E-mail address: fgutier@unizar.es (F. Gutiérrez).

https://doi.org/10.1016/j.geomorph.2024.109545
Received 23 October 2024; Received in revised form 2 December 2024; Accepted 2 December 2024
Available online 4 December 2024

pre-existing discontinuities (bedding, joints, faults), high-relief and steep slopes, glacial debuttressing, fluvial undermining and down-cutting, large earthquakes and topographic amplification of seismic shaking, or humid climate conditions (Margielewski, 2006b; Agliardi et al., 2009a, 2009b; Pánek et al., 2011; Crosta et al., 2013; Starkel et al., 2013; Chalupa et al., 2018; Březný et al., 2021; McCalpin and Jones, 2021).

The flysch Outer Western Carpathians (OWC) in the Czech Republic represents the hilly or mid-mountain region where DSGSDs occur at their lower limit, in terms of local relief and slope gradient (Chalupa et al., 2018; Pánek et al., 2019; Chalupa et al., 2021). Here, the majority of the DSGSDs exhibit a limited degree of geomorphic development, reflected by the scarce diversity and number of diagnostic landforms. Previous studies have revealed suitable structural conditions in the flysch terrain of the Czech OWC, with tectonic and lithological anisotropies prone to the development of DSGSDs (Novosad, 1966; Nemčok, 1982; Pánek et al., 2011; Chalupa et al., 2018, 2021). A number of studies illustrate that in the OWC the initiation and activity of DSGSDs and landslides are closely linked to the specific climatic conditions and variations occurred during the Pleistocene/Holocene transition and the Holocene (Margielewski, 2006b; Pánek et al., 2011; Chalupa et al., 2021).

The aim of this study is to illustrate a multidisciplinary approach for the morpho-structural and evolutionary characterization of DSGSDs, integrating surface and subsurface data gathered by means of LiDAR-based detailed geomorphological mapping, structural analysis, geophysical surveying including electrical resistivity tomography (ERT) and ground-penetrating radar (GPR), and trenching in combination with radiocarbon and optically stimulated luminescence (OSL) dating. The approach, tested in a complex DSGSD on Travný Mt. (Moravskoslezské Beskydy Mountains, Czech Republic), allows inferring essential data for the characterization of DSGSDs and the assessment of the associated hazard, including: (1) extent of the area affected by gravitational ground deformation; (2) internal structure, deformational mechanisms and depth; (3) main predisposing and potential triggering factors; (4) kinematic style (progressive versus episodic); and (5) timing of displacement episodes, particularly the most recent event. The work provides new geochronological data for the poorly dated DSGSDs of the OWC (Margielewski, 2006b; Pánek et al., 2011; Chalupa et al., 2021).

2. Regional setting

2.1. Structure and geology of OWC

The study area of Travný Mt. is located within the Moravskoslezské Beskydy Mountains (MSB, eastern part of Czechia; see Fig. 1A for location), which is the highest part of the Czech OWC, with elevations reaching >1300 m a.s.l. (Fig. 1B). From the geological perspective, the MSB corresponds to a thrust sheet consisting of a >1.5 km thick Upper Cretaceous to Oligocene flysch succession. This nappe was transported toward the NW during Miocene times, overthrusting foredeep Miocene (Badenian, ~15 Ma old) sediments, which unconformably overlie the Paleozoic basement (Menčík et al., 1983). The highest ridges of the MSB are mainly composed of resistant, thick-bedded (even >10 m), sandstone-dominated flysch of the Silesian Unit (SU). The flysch bedrock of the SU displays a general isoclinal structure with a gentle S to SE dip lower than 20°, locally complicated by folds and a dense pattern of faults (Menčík et al., 1983; Menčík, 1989). The topography, with an overall cuesta-type landscape, is largely controlled by the isoclinal structure and the variable resistance of the flysch units. The ridges commonly display gentle ~SSE-facing concordant dipslopes controlled by resistant units, and steep ~NNW-facing anti-dip slopes (Fig. 1B). The main ENE–WSW trending ridge is deeply incised by valleys controlled by NNW–SSE oriented transverse fault zones (Menčík et al., 1983; Menčík and Tyráček, 1985). These discordant drainages are flanked by high (up to 750 m) orthoclinal slopes.

Travný Mt. (1203 m a.s.l.) is one of the highest peaks of the main ridge (Fig. 1B). The analysed DSGSD is located on the ENE-facing slope of Travný Mt., at the margin of the valley excavated by the transverse Morávka River (Figs. 1B and 2A). The hillslope has a local relief of ~600

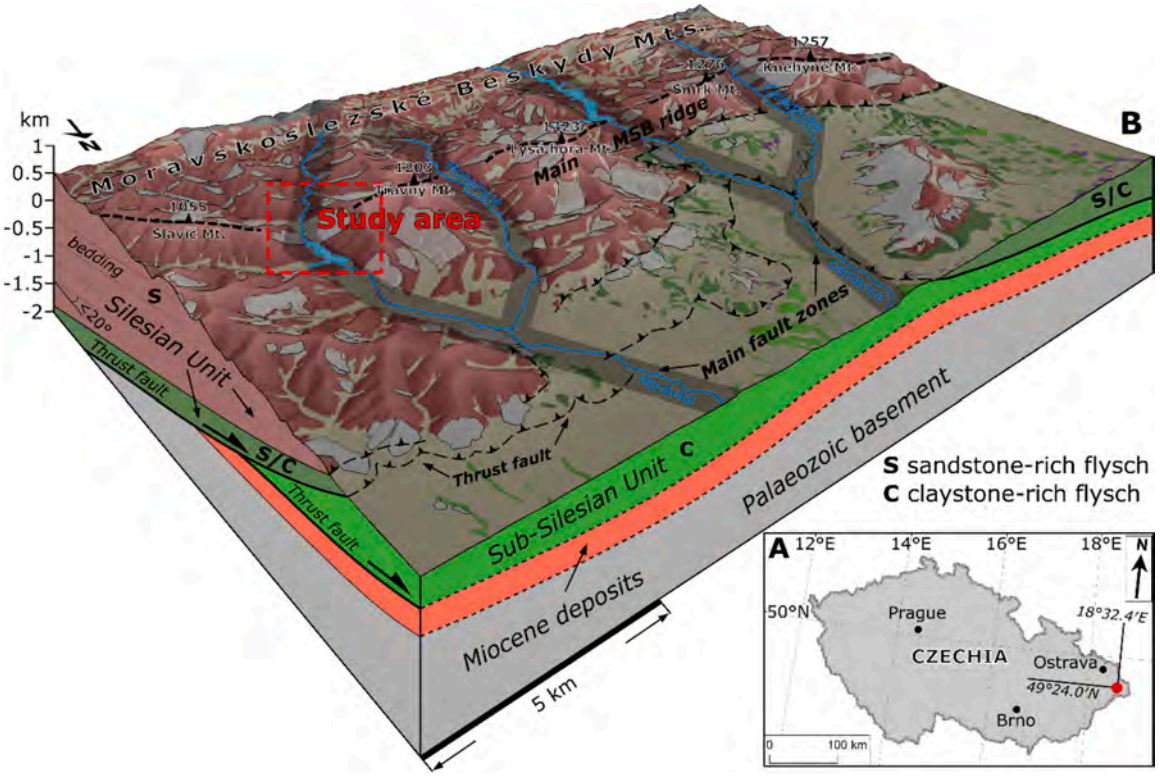

Fig. 1. A) Location of the study area. B) Simplified geology and structure of the Moravskoslezské Beskydy Mts.

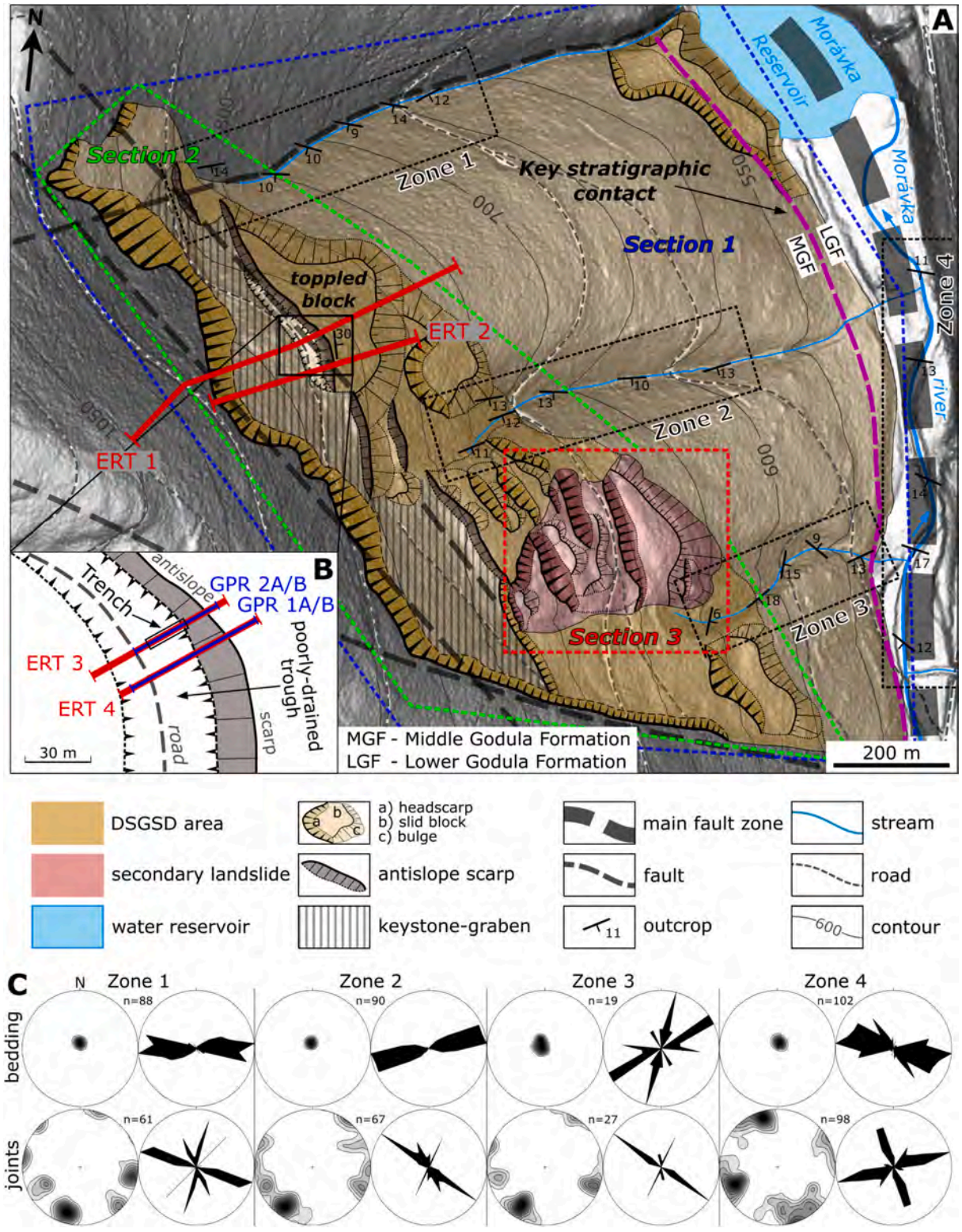

Fig. 2. A) Geomorphological map of study area showing the main geological and structural features. The purple line represents the stratigraphic contact between the relatively weak Lower Godula Formation (LGF) and the more competent Middle Godula Formation (MGF). The location of the geophysical (ERT) profiles is indicated. Note that the Morávka Dam is located approximately 1.3 km to the northwest of the study area. B) Detailed sketch of the selected trenching site with layout of geophysical lines (ERT, GPR) and trench. C) Structural measurements plotted in rose diagrams (strike) and lower hemisphere stereographic projections (poles of planes).

m and a mean gradient of around 30°. The flysch bedrock has a dominant strike approximately perpendicular to the slope orientation and a gentle SSE dip of 9–18°, consistent with the general isoclinal structure of the Silesian Unit. The flysch succession includes two conformable formations, from top to base: (1) the Turonian-age Middle Godula Formation (MGF), which underlies most of the slope and consists of relatively thick (<1 m) and competent beds of coarse-grained sandstone interbedded by occasional thin layers (<10 cm) of mudstone; and (2) the mechanically weaker Cenomanian-Turonian-age Lower Godula Formation (LGF), located in the lowermost part of the slope and made up of thinly bedded (<10 cm) fine-grained sandstones and mudstones with some competent sandstone interbeds of moderate thickness (<1 m). The portion of the slope affected by the DSGSD, mapped on the basis of geomorphic evidence, is 1.5 km long, 1.3 km wide and covers ~1.2 km^2. Its upper edge is expressed by a well-defined headscarp ~2 km long and the slope movement extends from 970 m a.s.l. to the valley floor at 500 m a.s.l., with a maximum local relief of 470 m (Fig. 2A). Geotechnical investigations carried out during the construction of Morávka Dam, located 1.3 km to the NE of the analysed DSGSD (see upstream sector of the reservoir in Fig. 2A), revealed extensive deep-penetrating gravitational disruption in the bedrock (Novosad, 1966), pointing to the existence of a morphologically indistinctive slope deformation affecting a larger area than that identified in our geomorphological map, probably covering the whole ENE slope of Travný Mt.

3. Materials and methods

3.1. Structural and landform analyses

To obtain relevant data on the structure of the flysch bedrock, 552 dip measurements (direction and value) on bedding planes (299) and joints (253) were collected with a compass. The data were obtained in 24 stations located within the DSGSD and in undisturbed nearby areas. All measurements were grouped according to their topographic location, structural position and lithology (Fig. 2A, C). Four zones (Fig. 2A, C) were differentiated for the graphic representation of the data, corresponding to three drainages that dissect the slope (Zones 1–3) and exposures associated with the Morávka River channel (Zone 4). Structural data from stratification planes and joints were projected separately for each zone in stereographic nets on lower hemisphere (pole of planes) and rose diagrams (strike) (Fig. 2C). Additionally, structural data from distant areas depicted in the existing geological maps were taken into consideration (Menčík and Tyráček, 1985; Menčík, 1989; Czech Geological Survey, 2004). The limited outcrops in this heavily forested area did not allow us to gather any data on tectonic faults. Nonetheless, a LiDAR-based recognition of tectonic lineaments was performed.

The boundaries of the DSGSD and the associated landforms were mapped using detailed relief models generated from a LiDAR-derived Digital Elevation Model (DEM). This DEM, provided by the State Administration of Land Surveying and Cadastre of the Czech Republic (DMR5G; State Administration of Land Surveying and Cadastre, 2017), has a spatial resolution of 1 m and a maximum elevation error in forested areas of 0.3 m. Geomorphic mapping was performed in a GIS environment using hillshade, slope gradient and aspect models derived from the DEM. In a subsequent stage, field surveys were carried out to verify and refine the cartographic information, as well as to better understand local geomorphic features and their relationship with the geological structure.

3.2. Trenching and dating

An 8 m long trench was excavated across the NW-SE-oriented antislope scarp and the associated poorly-drained trough located in the upper-northwest part of the DSGSD (Fig. 2A, B). The main aims of the trenching investigation were to (1) characterise the near-surface deformation style associated with the antislope scarp, (2) unravel the kinematic regime (progressive versus episodic), and (3) constrain the timing of the most recent deformation events. The trench walls were cleaned and an orthogonal reference grid with a spacing of 1 m was placed on the northern wall. The selected wall was logged on graph paper at a 1:50 scale. After interpreting the stratigraphic and structural relationships and inferring the displacement events, samples were collected for optically stimulated luminescence (OSL) and radiocarbon dating.

The two OSL samples (TN-06, TN-08) were collected by driving opaque PVC tubes horizontally into the deposit preventing exposure to light. Additionally, bulk sediment samples were obtained from around the sampling point for measuring the radionuclide concentration used for dose rate calculation. Ages were estimated using the relation Age (ka) = Equivalent dose (Gy)/dose rate (Gy/ka). Total dose rates were assessed: (1) measuring the activity concentrations of ^{238}U, ^{232}Th and ^{40}K by high resolution gamma spectrometry (Radioisotopes Unit, University of Seville) (Table 1) and applying appropriate conversion factors (Guérin et al., 2011); (2) considering the water content of the samples on arrival at the laboratory plus a 5 % error, to account for radiation attenuation; and (3) calculating the contribution of cosmic radiation as a function of latitude, altitude, burial depth, and average overburden density, based on data from Prescott and Hutton (1994). Final dose rate values were calculated using DRAC calculator (Durcan et al., 2015) (Table 1). Equivalent dose values were derived from the OSL response of quartz grains of sizes 150–250 μm extracted from each sample. Forty multi-grain aliquots of each sample were measured using a SAR blue OSL protocol (University of Cologne, Germany). Dose distributions showed over-dispersion values lower than 30 % when outliers were excluded. Outliers have been identified as those values outside 1.5 times the interquartile range. The burial dose was estimated using the central age model (CAM, Galbraith et al., 1999) on the reduced (i.e. without outliers) distributions. The ages were calculated using the relation indicated above, and are expressed in kiloyears before 2019 and with a 1 sigma error margin (Table 1).

The two samples collected for radiocarbon dating (TR1, TR2) were obtained from a thin organic-rich unit. Charcoal and conifer needles were dated at Beta Analytic (London BioSience Innovation Centre, UK). Details on the protocol used at Beta Analytic can be found in Moreno et al. (2021). The obtained AMS radiocarbon ages were calibrated by Beta Analytic using the high probability density range method (BetaCal3.21) and the database Intcal13 (Reimer et al., 2013) (Table 2).

3.3. Geophysical surveying

Electrical resistivity tomography (ERT) was applied in order to gain insight into the internal tectonic and gravitational structure of the DSDSD. The main aims were to: (1) investigate the gravitational structures responsible for the slope deformation, expressed in the landscape as scarps and troughs; (2) explore geometrical relationships between the DSGSD and the predisposing structural features of the bedrock, and (3) constrain the extent and depth of the DSGSD. In total, four ERT profiles (ERT 1–4, Fig. 2A, B) were acquired. All of them were located in the upper part of the DSGSD at its northern sector, with WSW-ENE orientation subparallel to the general strike of the flysch bedrock and perpendicular to the scarps and depressions. The long ERT 1 and 2 sections were placed across the upper keystone-graben depression, extending from undisturbed ground above the headscarp to the footwall of the main antislope scarp (toppled block). The short ERT 3 and 4 sections were located across the poorly-drained trough situated at the foot of the main antislope scarp, where the trench was excavated. The central sector of ERT 3 coincides with the trench site.

The Wenner-Schlumberger (W–S) array was selected because of its ability to capture both vertical and horizontal structures with sufficient resolution and its low sensitivity to geoelectric noise (Loke, 1997; Zhou et al., 2002; Szalai and Szarka, 2008; Szalai et al., 2009). The data were acquired with an ARES system (by GF Instruments) using 12

Table 1
Radionuclide activity concentration measured by high resolution gamma spectrometry, sample depth, assigned water content, total dose rate, and estimated equivalent doses used for age calculation.

Sample	Lab code Cologne/ Sevilla	Depth (m)	Moisture (%)	^{40}K (Bq/ kg)	^{232}Th (Bq/ kg)	^{238}U (Bq/ kg)	Dose rate (Gy/ ka)	Burial dose (Gy)	Age (ka before 2019)
TN-06	C-L4939 3677	1.5	28 ± 5	563 ± 26	32 ± 1	24 ± 1	2.37 ± 1.1	23.4 ± 1.1	9.9 ± 0.6
TN-08	C-L4940 3678	1.2	28 ± 5	548 ± 25	27 ± 2	18 ± 1	13.2 ± 0.7	13.2 ± 0.7	6.1 ± 0.4

Table 2
Radiocarbon dating. Sample code, laboratory number provided by Beta Analytic, material, conventional ages and calibrated ages with an error margin of two sigma using the high probability density range method (BetaCal3.21) and the database Intcal13 (Reimer et al., 2013). Figures in parentheses indicate the relative area under the probability curve. More probable age ranges with relative areas ≥80 % are indicated in bold. BP refers to years before 1950.

Sample	Laboratory number	Material	Conventional age ^{14}C (yr BP) or percent modern carbon (pMC)	Calibrated age (2σ) (yr AD)	Calibrated age (2σ) (yr BP)
TR1	Beta – 539536	Charcoal	140 ± 30	1669–1780 (43.1 %) 1798–1891 (36.8 %) 1908–1944 (15.5 %)	281–170 (43.1 %) 152–59 (36.8 %) 42–6 (15.5 %)
TR2	Beta – 539537	Conifer needles	145.64 ± 0.54 pMC	*1972–1973* (*84.3* %) 1962 (8.4 %) 1971 (2.8 %)	

multielectrode cable sections 40 m long, each including 8 electrodes. Thus, the maximum measurable length with simultaneously connected electrodes was 475 m. The "roll along" approach was applied to measure longer profiles. The theoretical penetration depth is ~1/5 of the maximal distance covered by simultaneously connected current electrodes (Loke, 1997). The raw datasets were processed using the Res2Dinv software (Loke and Barker, 1996). Measured apparent resistivity data were manually checked, removing poor quality data points. Then, the least-squares inversion method was used. Detailed specifications of the ERT surveys are presented in Table 3.

Ground-penetrating radar was applied at the poorly-drained trough selected for trenching, with the aim of obtaining additional information on shallow deformation structures and sedimentary features (i.e., larger extent and penetration than the trench). A MALÅ system with 80 and 160 MHz shielded antennas was used. Data was collected across the trough along two lines replicating the profiles with the two antennas. Profiles GPR1A/B largely coincide with section ERT 4, and profiles GPR 2A/B cover the trench and part of section ERT3 (see Fig. 2B for location). GPR data were processed using ReflexW (Sandmeier software, 2019). We applied time zero correction, 2D and 1D filtering (background removal, average subtraction, bandpass filters) and gain functions to enhance GPR images and filter out undesired noise. Specifications of GPR profiling are presented in Table 4.

4. Results and interpretations

4.1. Geology and landforms

The DSGSD covers 1.18 km^2 of an ENE-facing orthoclinal slope at the left side of the deeply entrenched (>600 m) Morávka River valley. It covers an elevation range of 500–970 m a.s.l., has a local relief 100–460 m and a slope gradient of 15–35°. The DSGSD can be divided into three overlapping sections (DSGSD Sections 1–3, see Fig. 2A) suggesting three

Table 3
Parameters of the ERT sections.

Profile number	Electrode array	Electrode spacing (m)	Profile length (m)	Penetration depth (m)	RMS error (%)
1	W-S	5	675	~100	10.2
2	W-S	5	395	~85	9.8
3	W-S	1	63	~12	9.5
4	W-S	0.5	63.5	~8	2.8

Table 4
Parameters of the GPR profiles.

Profile number	Antenna type (MHz)	Profile length (m)	Penetration depth (m)
1a	80	55	~18
1b	160	55	~13
2a	80	32	~21
2b	160	32	~13

potential phases of activity. Section 1 represents the original body of the DSGSD from below the headscarp to the valley floor, laterally defined by well-defined northern and southern boundaries. It is a compact block-like body, almost featureless with minor scarps and toe bulging (Fig. 2A). Here, the river was deflected eastward and the valley was narrowed by DSGSD activity. Absence of DSGSD landforms in this sector suggests an advanced stage of degradation, pointing to a long period of inactivity. Section 2, situated in the upper south-western part, displays conspicuous landforms typical of DSGSD and represents a key area for this study. Its upper boundary is defined by a ~2 km long and 10–30 m high headscarp with slope gradients >55°. Below, the slope is ruptured by several NNW/NW–SSE/SE-oriented antislope scarps with an overall left-stepping arrangement. The headscarp (Fig. 3B) and the en-echelon antislope scarps bound a graben depression partially filled by coarse colluvium (Fig. 3A). The poorly drained trough investigated by trenching and geophysics is situated in the northern part of the graben depression, at the foot of the main uphill-facing scarp. Below the antislope scarps there are several rotated and toppled blocks with associated secondary scarps (Figs. 2A, 3A). Section 2 is ascribed to a second phase of activity. Section 3, located on the southern sector of the DSGSD, shows the most conspicuous and less degraded landforms corresponding to a secondary superimposed landslide that represents the youngest partial reactivation. In this section, the slope displays several scarps, numerous rotated blocks, hummocks and a deflected gully (Fig. 2A).

The slope affected by the DSGSD consists of two lithologically, structurally and mechanically distinct flysch units separated by a conformable stratigraphic contact. The upper and middle part of the slope is underlain by the MGF, made up of competent medium-to-thick (0.1–1 m) coarse sandstone beds with occasional thin (<0.1 m) mudstone and sandstone interbeds. This unit shows a general isoclinal attitude with average dip direction/dip of 175°/12° (i.e., strike subperpendicular to the slope orientation). In the southern sector, this upper competent unit is locally folded and the attitude of the bedding is

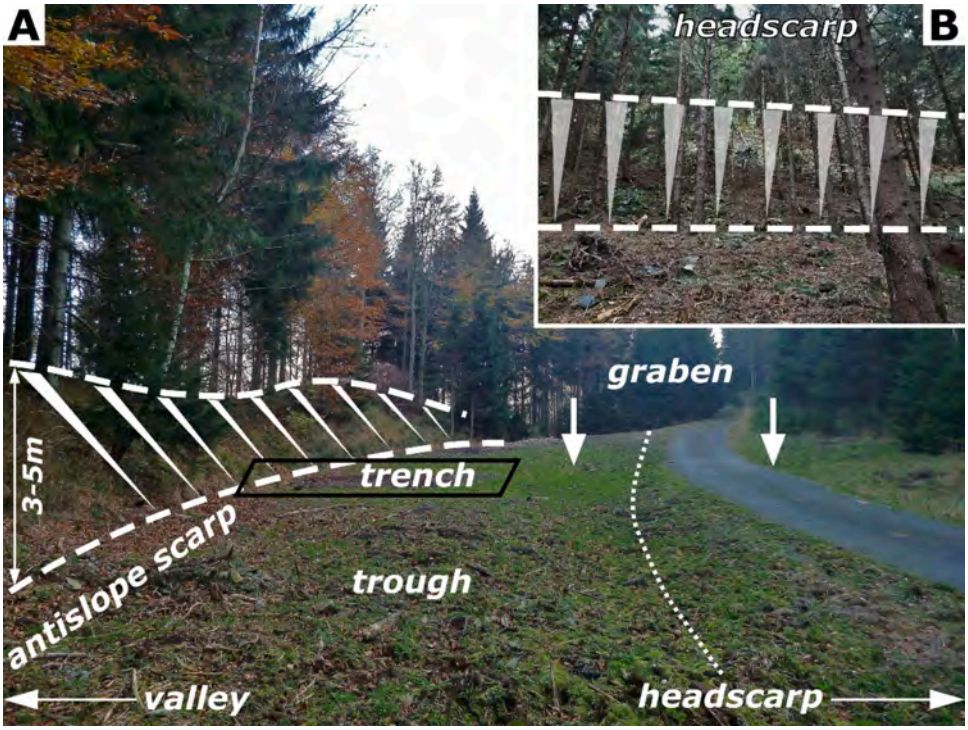

Fig. 3. Images of selected landforms. A) Antislope scarp and graben depression. B) Main headscarp.

more variable with a range in the dip direction and dip ~40–130° and 10–20°, respectively (Zone 3). The lower part of the slope and the Morávka valley are underlain by the LGF, characterised by mechanically weak, thinly bedded (<0.1 m) sandstones and mudstones with rare intercalations of thicker (<1 m) sandstone beds. This unit also shows an overall SSE-dipping isoclinal attitude with dominant dip direction and dip values of 190–200° and 10–20°, respectively. A structurally different unit is represented by the toppled block associated with the main antislope scarp in the upper part of the DSGSD, where the gravitationally rotated beds show an anomalous dip direction of 70°–90° subparallel to the slope orientation and outward dips of 20–40° (see Fig. 2A, C). Both the MGF and the LGF are separated by a well-defined stratigraphic contact at the base of the slope, although poorly exposed (Fig. 2A). The whole massif is densely fractured by subvertical joint sets with dominant NNW/NW–SSE/SE, WNW–ESE and WSW–ENE trends. The joint spacing and penetration depth are significantly larger in the upper competent flysch unit. A number of faults have been documented. The main fault zone with NNW/N–SSE/S trend controls the path of the Morávka valley. A NW–SE oriented fault can be inferred along the DSGSD headscarp in the upper part of the slope. Both faults are crossed by two of faults with WSW–ENE and WNW–ESE strikes along the northern and southern edges of the DSGSD, respectively. These faults compartmentalize the rock massif into a wedge-like block that determine the extent of the DSGSD (see Fig. 2A).

4.2. Trenching and dating

The trench with N55E orientation was excavated perpendicularly to the margin of the graben depression and extending along the lower part of the NW–SE-oriented antislope scarp and the linear trough lying at its foot, within Section 2 of the DSGSD (see Figs. 2A, B and 3A for location). The antislope scarp, underlain by sandstone-dominated flysch bedrock, reaches a height of 5 m some tens of meters south of the trench. The trough has a longitudinal NW-directed gradient and currently behaves as an externally drained depression with an outlet that connects with the gully that defines the northern edge of the DSGSD (Figs. 2A, 3A).

The trench essentially exposed old trough deposits juxtaposed against flysch bedrock by a normal fault contact with an associated shear zone, and non-deformed younger deposits that onlap the bedrock and truncate the fault. The stratigraphic units exposed in the trench can be divided into four groups separated by major discontinuities (i.e., faults, unconformities). Detailed descriptions of the units and the shear zones are included in Fig. 4.

The footwall bedrock, exposed beneath the lower part of the scarp, consists of competent sandstone beds with thin clay partings (Subunit 1). The bedding gently dips toward the valley, suggesting some toppling of joint-bounded blocks (dip direction/dip 94°–108°/14°–17°). These sediments display a penetrative set of NW–SE-oriented joints steeply (≥70°) dipping into the slope. The fresh bedrock abruptly changes into a crackle breccia next to the shear zone (Subunit 1B), forming part of the fault damage zone.

The lowermost package of the faulted trough fill includes units 2 and 3. Unit 2 corresponds to colluvium with abundant cobbles which long axes prevalently dip toward the trough. Unit 3 is a texturally more mature facies made up of moderately sorted pebble gravel, most probably deposited by overland flow focused along the axis of the depression.

Unit 4 is a faulted colluvial wedge that reaches 1.3 m in thickness at its proximal edge, defined by a subvertical fault contact with the relatively loose shear zone SZ3. Its base shows a nearly horizontal discordant contact with the underlying unit 2, roughly dipping toward the trough as indicated by the fabrics of the cobbles. The deposit of the colluvial wedge consists of massive, cohesive silty sand with floating subequant angular pebbles. A sample collected 0.2 m above the base of the unit in its middle-distal sector yielded an OSL age of 9.9 ± 0.6 ka.

The non-deformed unit 5 extends along most of the trench, onlapping the bedrock and with its base clearly truncating the fault zone. This unit is composed of colluvial, matrix-rich angular gravel beneath the slope (Subunit 5C) that grades into fluvial-like facies of subrounded and moderately sorted gravels ascribable to water flows channelled along the trough. A sample collected in the fluviatile facies 0.4 m above the base of the unit has yielded an OSL age of 6.1 ± 0.4 ka. Units 6, 7 and 8 are restricted to the bottom sector of the trough, probably filling a shallow erosional channel. Unit 6, consisting of a thin layer of dark clay with abundant organic material, drapes a trough-like paleotopography.

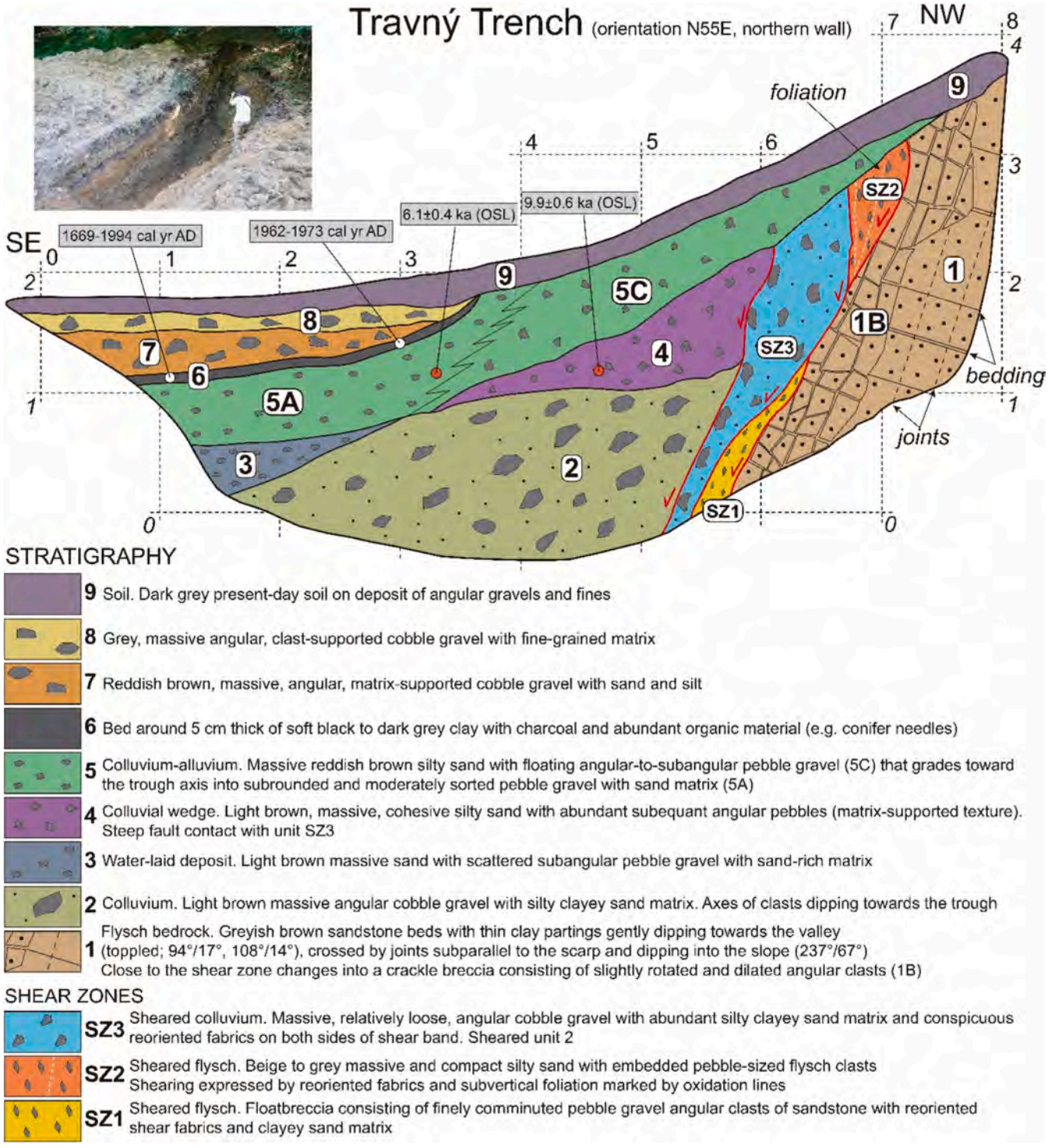

Fig. 4. Log of trench T1. Scale in meters. See location in Figs. 2 and 3.

A charcoal sample and conifer needles collected from this unit provided calibrated radiocarbon ages of 1669–1944 cal yr AD and 1962–1973 cal yr AD, respectively. This unit records a period of poor drainage conditions attributable to natural or anthropogenic factors, such as impeded drainage by aggradation (e.g., debris flow accumulation) or artificial ponding. Units 7 and 8 are massive matrix-rich deposits of angular cobble gravel ascribable to recent debris flow events. The topographic surface is underlain by a laterally continuous dark grey soil developed on fine-grained material with angular gravels.

The 0.6–1 m wide shear band situated between the faulted downthrown deposits of the trough fill (units 2, 4) and the brecciated bedrock (subunit 1b) shows an overall 60°–70° dip toward SW and comprises three distinctive zones. SZ1 and SZ2 are finely comminuted flysch consisting of fine-grained material with subvertical foliation and pebble-sized clasts showing reoriented fabrics. SZ3 seems to correspond to a sheared and dragged portion of unit 2.

The stratigraphic and structural relationships observed in the trench allow inferring a minimum of two surface rupturing events associated with the development of the antislope scarp and the accompanying trough. The first clearly discernible rupture event (penultimate event;

PE) is recorded by the colluvial wedge abutting the shear zone. Displacement along the fault steeply dipping into the slope created an unstable antislope scarp. The degradation of the antislope scarp at least partially underlain by unconsolidated material resulted in the accumulation of the colluvial wedge. The thickness of the colluvial wedge provides a minimum estimate of 1.3 m for the vertical displacement of this event, and suggests a value of 2.6 m considering the rule of thumb whereby vertical displacement is often around two times the thickness of colluvial wedges (McCalpin, 2009). The most recent event (MRE) is recorded by faulting of the colluvial wedge. The proximal edge of the colluvial wedge was recognized as a fault contact, rather than a buried fault scarp, considering: (1) its steep attitude, locally higher than the fault section below; (2) the clear shear fabrics shown by the shear zone SZ3; and (3) the loose nature of SZ3, which could not maintain a steep scarp. In this case, the thickness of the colluvial wedge also provides a minimum measure of the vertical displacement occurred in the MRE. The lack of a second colluvial wedge related to this event could be related to factors such as: (1) the development of a complex deformational topography involving other major surface ruptures in the footwall; (2) a free face scarp underlain by bedrock; and (3) significant erosional removal of the deposits shed from the putative scarps along the inclined trough axis. The timing of both the PE and the MRE can be bracketed at 10.5–5.7 ka by the OSL ages and their uncertainties obtained from units 4 and 5, assuming that the colluvial wedge was deposited soon after the penultimate event. The oldest OSL age of 9.9 ± 0.6 ka can be considered as a good approximation for the PE, since it can be assumed that the colluvial wedge was deposited soon after the surface rupture. Most probably, other additional older events have been involved in the development of the antislope scarp and the trough, which may accumulate a vertical displacement significantly >8.5 m, considering the height of the scarp (ca. 5 m) affected by erosion and the minimum thickness of the exposed faulted sediments (3.5 m).

4.3. Geophysical structure of DSGSD

The SW–NE-oriented ERT 1 profile was placed in Section 2 of the DSGSD, traversing the headscarp, the graben depression, the trough associated with the antislope scarp (trenching site), and the toppled block situated on its NE margin (Fig. 2A). In the upper part above the headscarp, the profile shows electrolayers with contrasting resistivity attributable to gently dipping undisturbed bedrock consisting of alternating sandstone-dominated (S1/2) and sandstone/claystone packages (S/C; see Fig. 5). At around station 140 m, above the headscarp, the resistivity image displays a sharp lateral resistivity change steeply dipping toward the valley, ascribable to the NW–SE-trending fault inferred from a terrain lineament crosscutting whole ridge (Fig. 2A). At station 190 m and coinciding with the headscarp, the main shear zone >100 m deep of the DSGSD and most probably controlled by the adjoining fault can be identified. Another shear zone steeply dipping into the slope can be also interpreted at the foot of the antislope scarp, at station 390 m, corresponding to the fault exposed in the trench. The high-resistivity anomalies beneath the antislope scarp accompanying shear zones (station 370–400) was interpreted as air-filled crevices. The master synthetic fault and the secondary antithetic fault, expressed in the landscape by the headscarp and the antislope scarp, bound a wedge-shaped downdropped block (keystone graben). The electrolayers on both sides of the shear zone associated with the headscarp show a vertical offset of around 30 m. A toppled block to the NE of the antislope scarp, with bedding significantly dipping toward the valley (measured in outcrops and in the trench), is inferred at least between stations 390–500 m (Fig. 5).

The profile ERT 2 provides a more detailed resistivity image of the keystone graben and the toppled block associated with the antislope scarp (Fig. 2A). The downthrown block and shear zones interpreted in profile ERT 1 are also captured in ERT 2 at stations 30 m (headscarp), 130 and 160 m (synthetic faults), and 200 m (antithetic fault associated with the antislope scarp). Also here, the air-filled crevices related to shear zones was documented. The complex resistivity pattern imaged beneath a high-resistivity colluvial mantle in the toppled block between stations 200–320 m, can be attributed to the compartmentalization of toppling blocks by a joint set subparallel to and steeply dipping into the slope, as measured in the structural stations and the trench. This toppling process is most probably accompanied by the gravitational fragmentation and dilation of the rock mass (Fig. 5).

The profiles ERT 3 and 4 were placed across the antislope scarp and the associated trough, overlapping the trench site and 15 m to the SE, respectively (Fig. 2B). These resistivity images capture: (1) the low-resistivity clayey fill of the externally drained trough, with a thickness of around 2–4 m; (2) the steeply dipping antithetic fault situated at the foot of the antislope scarp, expressed by a sharp lateral resistivity contrast; and (3) lateral resistivity variations NE of the trough (Fig. 5).

Two pairs of GPR profiles were acquired across the trough and the antislope scarp with 80 and 160 MHz shielded antennas. Profiles GPR2A/B overlapped the trench and largely coincide with section ERT 3, for direct comparison. Profiles GPR1A/B were collected along the trace of section ERT 4 (Fig. 2B). Overall, the quality of the radargrams is rather poor, and their ill-defined reflections are difficult to unambiguously interpret as stratigraphic or structural features. Nonetheless, all the profiles show a sharp lateral change in the reflection pattern at the foot of the antislope scarp ascribable to the fault and associated shear zones exposed in the trench (stations 20 and 13 in GPR 1 and 2, respectively). Both the base of the trough fill and its internal stratigraphy are difficult to resolve, most probably due to the massive and rather homogeneous character of the different units, with boundaries that do not represent significant changes in the electromagnetic properties. The boundaries of the units identified in the trench have been depicted in an enlarged excerpt of profile GPR 1B. The right part of profiles corresponds to the toppled block with complex and difficult to interpret reflection patterns (Fig. 6).

5. Discussion

5.1. Preconditions and distribution of DSGSDs in the OWC

DSGSDs usually affect high-mountain regions with the steep slopes worldwide (Teshebaeva et al., 2019; Di Luzio et al., 2022). Compared to the documented areas with abundant DSGSDs such as the Alps (Agliardi et al., 2009a, 2009b; Crosta et al., 2013; Courtial-Manent et al., 2022), Pyrenees (Gutiérrez-Santolalla et al., 2005; Gutiérrez et al., 2008, 2012; Jarman et al., 2014; McCalpin and Corominas, 2019) and the Central (Nemčok, 1982; Pánek et al., 2017; McCalpin et al., 2019) or Southern (Gunnell et al., 2022) Carpathians, the Czech Outer Western Carpathians (OWC) represent the lower limit in the distribution of DSGSDs in terms of elevation and local relief, exhibiting a lower degree of geomorphic development. The majority of DSGSDs in high-mountain environments often show well developed morphology with multiple tiered antislope scarps, grabens and toe bulging, collectively affecting the landscape at mountain scale (Crosta et al., 2013; Jomard et al., 2014). Such a distinctive manifestation of DSGSDs is lacking in OWC. DSGSDs in OWC are mostly limited to individual landforms affecting small portions of the slopes. In mid-mountain relief, the DSGSDs are typically associated with tectonically active areas (Delano et al., 2018; Komura et al., 2020; Livio et al., 2022) or glacial debuttressing (Jarman, 2006; Bunkholt et al., 2013; Vick et al., 2020). DSGSDs in non-glaciated and tectonically inactive mid-mountain areas such as the OWC are rare (Alexandrowicz and Alexandrowicz, 1988; Kasprzak et al., 2016, 2019; Demurtas et al., 2021). Nonetheless, local litho-structural features in the flysch bedrock of the OWC provide favourable structural conditions for DSGSDs (Pánek et al., 2011, 2019; Březný et al., 2018a; Chalupa et al., 2021), even exceeding the often discussed factor of high-mountain relief (Crosta et al., 2013; Agliardi et al., 2019).

The Travný Mt. DSGSD represents the hillslope-scale complex

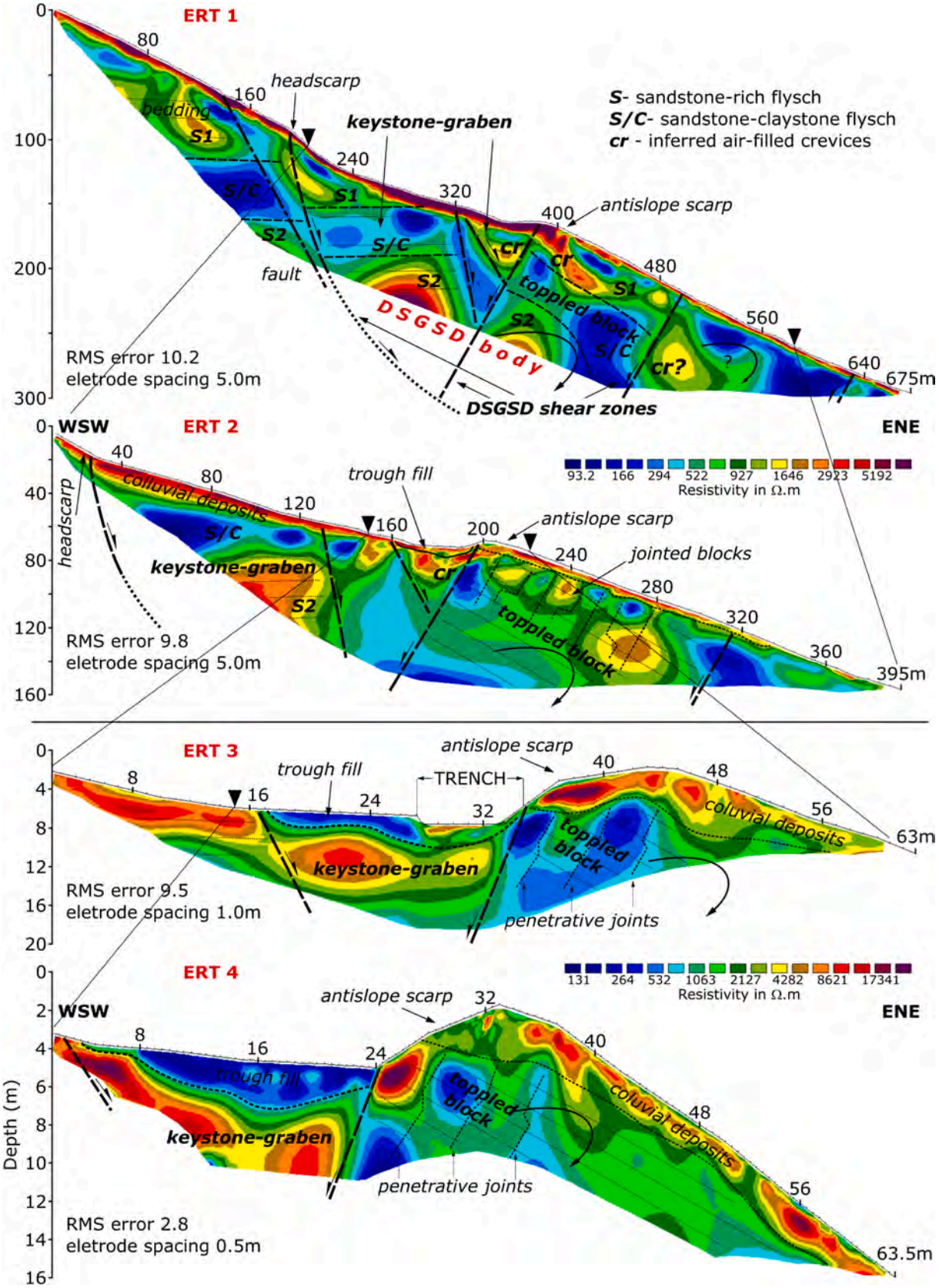

Fig. 5. ERT profiles. See location in Fig. 2.

deformation that likely exhibits multiple mechanisms. This gravitational deformation is expressed in the landscape by scarps, grabens, antislope scarps, and toe bulging (Agliardi et al., 2001; Gutiérrez-Santolalla et al., 2005; Jaboyedoff et al., 2013; Figs. 2A, 3). Its occurrence and deformation mechanism are controlled by the stratigraphic and structural features of the flysch bedrock at the site and the pre-existing structural-

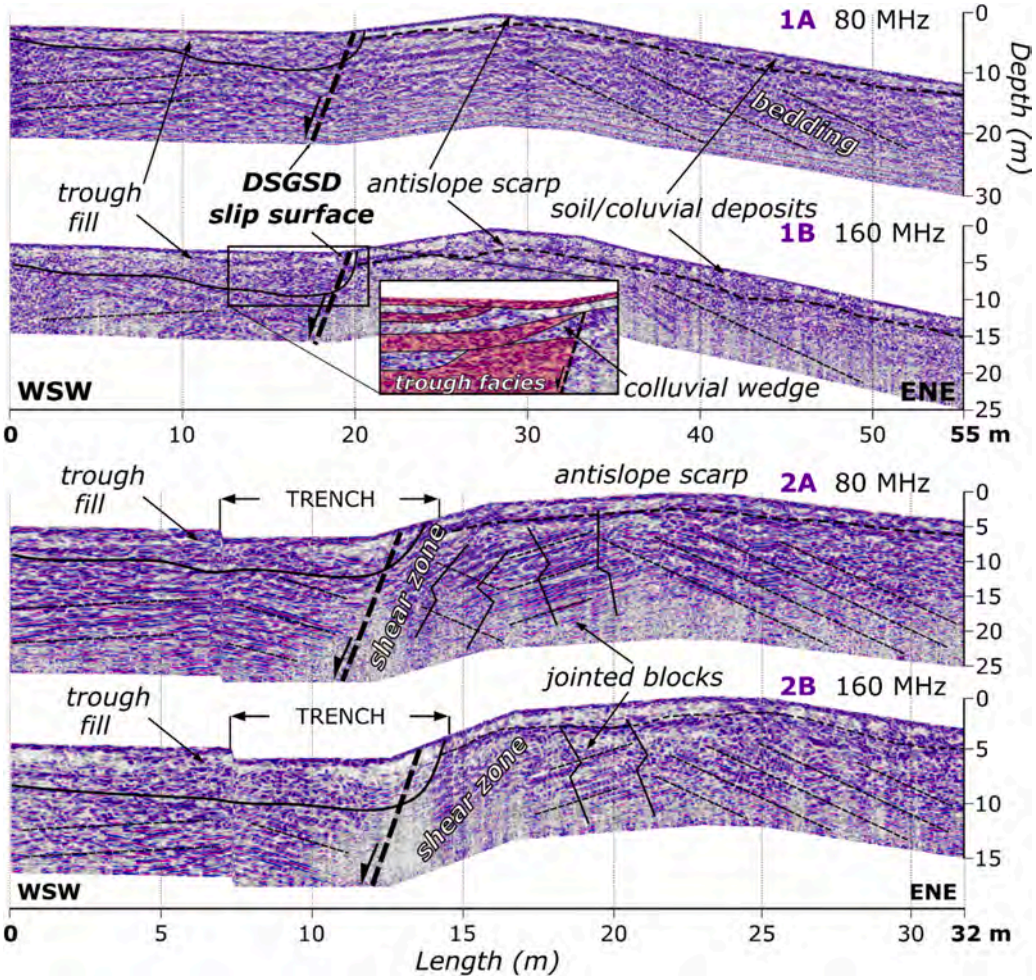

Fig. 6. GPR profiles. See location in Fig. 2.

tectonic elements. The initial instability was favoured by NW–SE, WSW–ENE and WNW–ESE trending faults, accompanied by a penetrative NW–SE joint set steeply dipping into the slope. The latter discontinuities compartmentalize the bedrock into elongated wedge-like blocks roughly parallel to the slope orientation (Březný et al., 2018a). The basal shear zone reaching a depth of >100 m is most probably associated with the stratigraphic-rheological contact between the competent and weak flysch formations (MGF and LGF) (Figs. 2A and 7B, C). These litho-structural factors are often discussed in the OWC (Pánek et al., 2011; Łajczak, 2014; Březný et al., 2018a; Pánek et al., 2019; Chalupa et al., 2021) as an essential precondition for DSGSDs. According to Pánek et al. (2011), the anisotropic flysch is strongly susceptible to deep-seated creep without distinctive morphological imprint ('intra-bed creep' sensu Novosad, 1966), documented also by Wagner et al. (1990) that documented air-filled crevices that weaken the rock massif (Fig. 5). The engineering geology study performed by Novosad (1966) in the Morávka Dam site confirmed such disruption in the vicinity of the analysed DSGSD. This suggests that DSGSDs can progress on a mountain scale below the surface without producing any recognizable landforms (Pánek et al., 2011; Březný et al., 2018a) (see Fig. 8A for location). Because of the presence of plastic claystone interbeds with low values of internal friction angle, translational sliding and spreading of competent sandstone can be accompanied by the development of air-filled crevices that weaken the rock massif (Novosad, 1966; Pánek et al., 2011). Novosad (1966) in the Morávka Dam site confirmed such deep-seated dislocation of sandstone blocks separated by a dense swarm of <1 m wide crevices reaching the valley floor, as documented in shafts dug during the construction of the dam in close vicinity to the study area. Similar crevices and ruptures have been interpreted within the deep structure of the analysed DSGSD (Fig. 5), suggesting rock mass damage of the whole massif (see Fig. 8A).

The DSGSDs in the MSB are clustered in the most elevated ridges (Pánek et al., 2011, 2019). In other parts of the OWC, hillslope-scale deep-seated deformations are rare (Bajgier, 1989; Margielewski, 2006a, 2006b). They mostly occur as gravitational collapses in isolated hills on nappe outliers (i.e., klippes) within the foothills, as documented by Chalupa et al. (2018) and Pánek et al. (2019) in Czech Podbeskydská Pahorkatina upland and Polish Beskid Wyspowy range sensu Alexandrowicz and Alexandrowicz (1988) and Margielewski (2006b). On the other hand, DSGSDs affects considerably higher mountain areas such as Babia Góra Mt. in Polish Western Carpathians (Łajczak, 2014; Łajczak et al., 2014; Kłapyta, 2020). The occurrence of DSGSDs in the MSB is predisposed by the litho-structural features of the bedrock in the hanging wall of a major thrust, which have played a crucial control on the development of the general topography and slope instability. During the nappe emplacement, the thick-bedded sandstone-dominated flysch (layers up to ~10 m) was affected by a network of NNW–SSE-trending faults. Although these faults are considered to be tectonically inactive nowadays (Menčík et al., 1983; Menčík, 1989), and most probably cannot seismically trigger the DSGSDs (Livio et al., 2022), we attribute to them two major controlling mechanisms. Firstly, the inherited faults and related joints, together with abundant discontinuities given by structural contacts and bedding, provide structural weaknesses dissecting the massif and controlling the gravitational movements (Agliardi et al., 2001; Pánek et al., 2011; Březný et al., 2018a; Chalupa et al., 2021). Secondly, the faults guided the path of the deeply entrenched

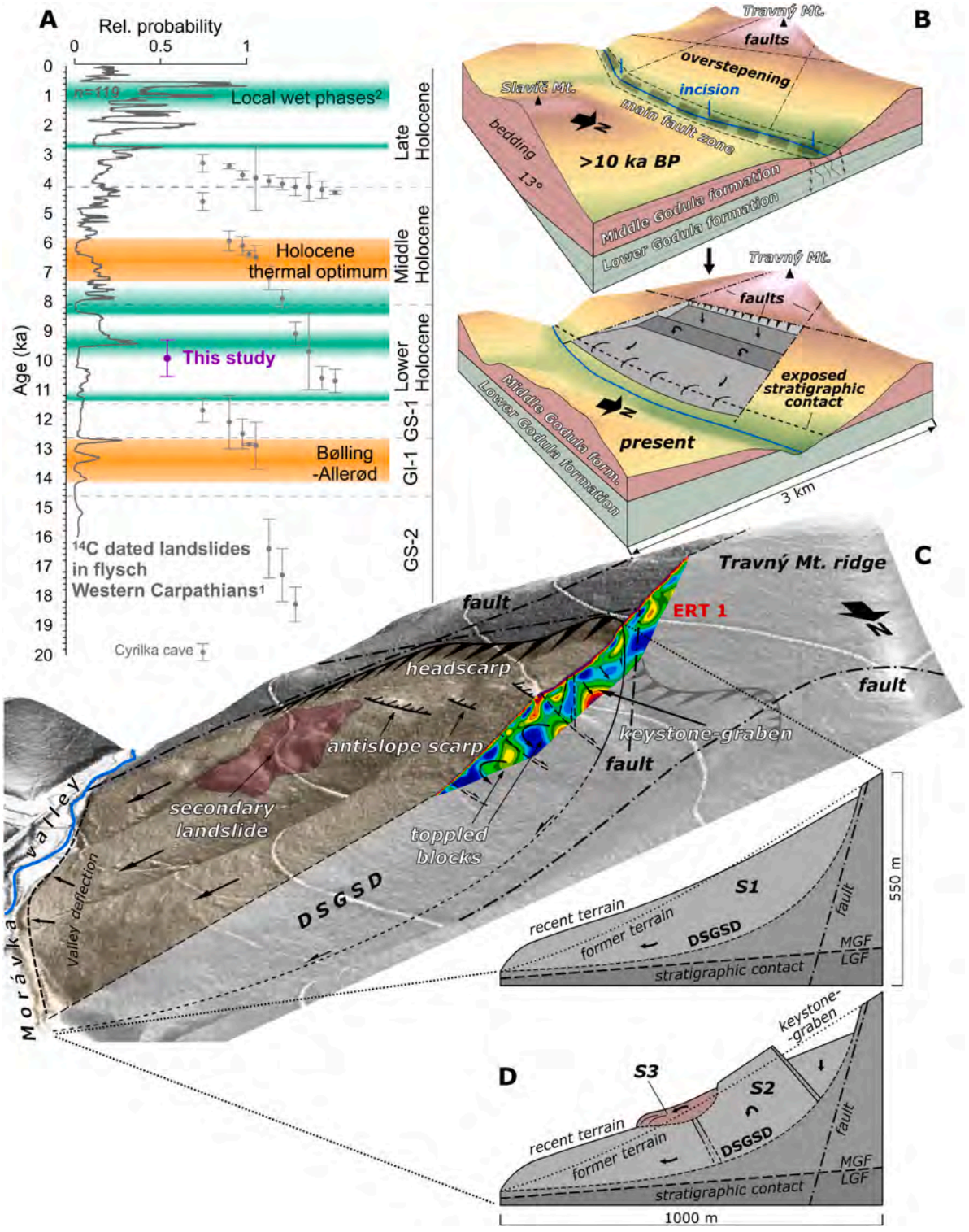

Fig. 7. A) Last Glacial-to-Holocene gravitational deformation activity in OWC. Grey points show ^{14}C, ^{10}Be and OSL ages of gravitational deformations from the Czech parts of OWC (Pánek et al., 2011; Břežný et al., 2018b; Lenart et al., 2018; Břežný et al., 2021; Chalupa et al., 2021). The curve on the left shows the relative probability of the ^{14}C ages of dated landslides in the Flysch Western Carpathians (based on data from Alexandrowicz and Alexandrowicz, 1999; Margielewski, 2003, 2006b; Margielewski et al., 2010, 2011; Pánek et al., 2013; Starkel et al., 2013; Pánek et al., 2014). Local climate patterns are adopted from Dabkowski et al. (2019). B) Schematic block diagram of structural-geological, tectonic and landform evolution of the study area. C) Visualisation of DSGSD and its internal structure in cross section and through the interpretation of the ERT 4 profile (resistivity same as on the Fig. 5). D) Simplified model of DSGSDs' evolution. Stage 1: initial instability; Stage 2: toppling and graben; Stage 3: shallow landsliding.

Morávka and Mohelnice rivers that dissect transversally the central MSB ridge (Fig. 8B), forming on the valley sides the highest slopes in the region (up to ~750 m). Such discordant valleys traversing the highest parts of the mountain range are rare within the OWC. Progressive increase in the slope height related to river downcutting could lead to the potential gravitational disturbance and ENE-directed displacement of

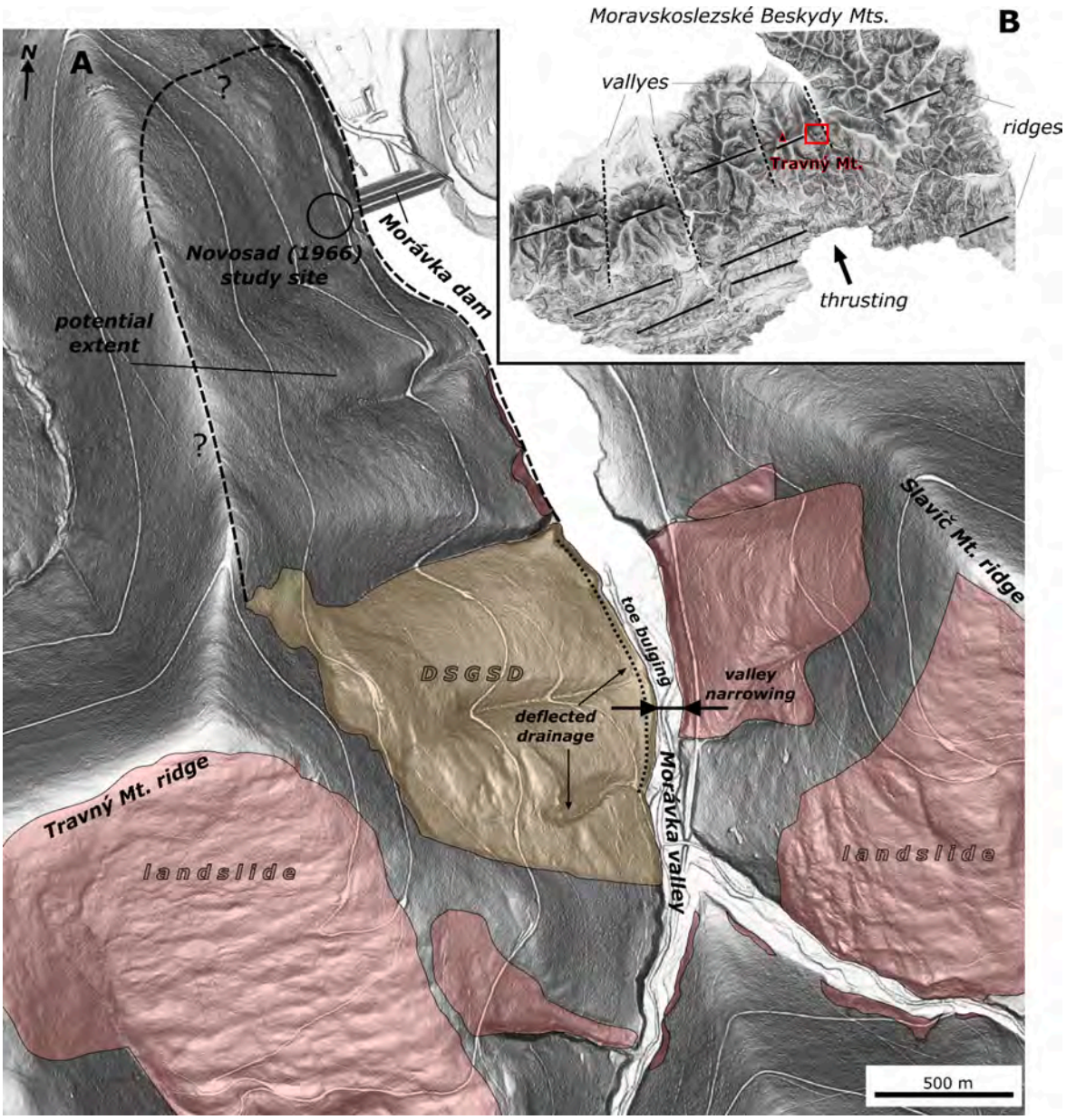

Fig. 8. A) Wider relations of study area and influence of DSGSD on drainage network. B) Overall landform arrangement in Moravskoslezské Beskydy Mts.

the Travný Mt., as was pointed by Březný et al. (2018a) the nearby the Smrk Mt. and supported by findings of Novosad (1966). Thus, the DSGSDs can be the local manifestation of such gravitational deformation in chronological order (1) segmentation of the mountain ridge by faults, (2) river downcutting and heightening of slopes, (3) valleyward extension and relaxation, (4) outward toppling of blocks and dip-slip displacement on fractures with favourable slope-parallel orientation (Fig. 7B, C, D). This interpretation is supported by the overall distribution of DSGSDs in the MSB with a dominant occurrence on the WSW- and ENE-oriented slopes (Fig. 9D). Thus, DSGSDs have both a topographical and a tectonic predisposition in central MSB.

5.2. Potential triggers and chronology of Travný Mt. DSGSD

Trenching is a valuable approach to learn about the initiation and history of DSGSDs, but may suffer from a number of limitations, including: (1) difficulties associated with carrying out excavations in remote mountain areas; (2) insufficient depth and length of the trenches; (3) dating limitations and uncertainties, (4) stratigraphic and structural relationships exposed in trenches may under-represent the deformation history of the investigated scarp, a more likely of the whole DSGSD. In a number of studies, it is implicitly assumed synchronicity in the formation and reactivation of all the scarps. However, recent trenching investigations suggest an upslope propagation in the formation of antislope scarps (e.g., Pánek et al., 2017; McCalpin and Corominas, 2019). Dating bedrock scarps by terrestrial cosmogenic nuclides (TCNs) provides valuable information the exposure history of the scarps (Hippolyte et al., 2009; Pánek et al., 2017), but is insufficient to reconstruct their kinematics differentiating rejuvenation events. Note that several processes in addition to surface deformation, such as erosion and aggradation, both operating at unknown rates, are involved in the exposure history of the scarps. Trough deposits may display difficult to interpret stratigraphy and structure, including contractional structures attributable to differential displacement within the DSGSD (e.g., greater forward displacement in upslope blocks than in the downslope ones; Pasquarè Mariotto and Tibaldi, 2016).

Within the OWC, trenching in combination with geochronological analyses, still represents a quiet unique and valuable method rarely used

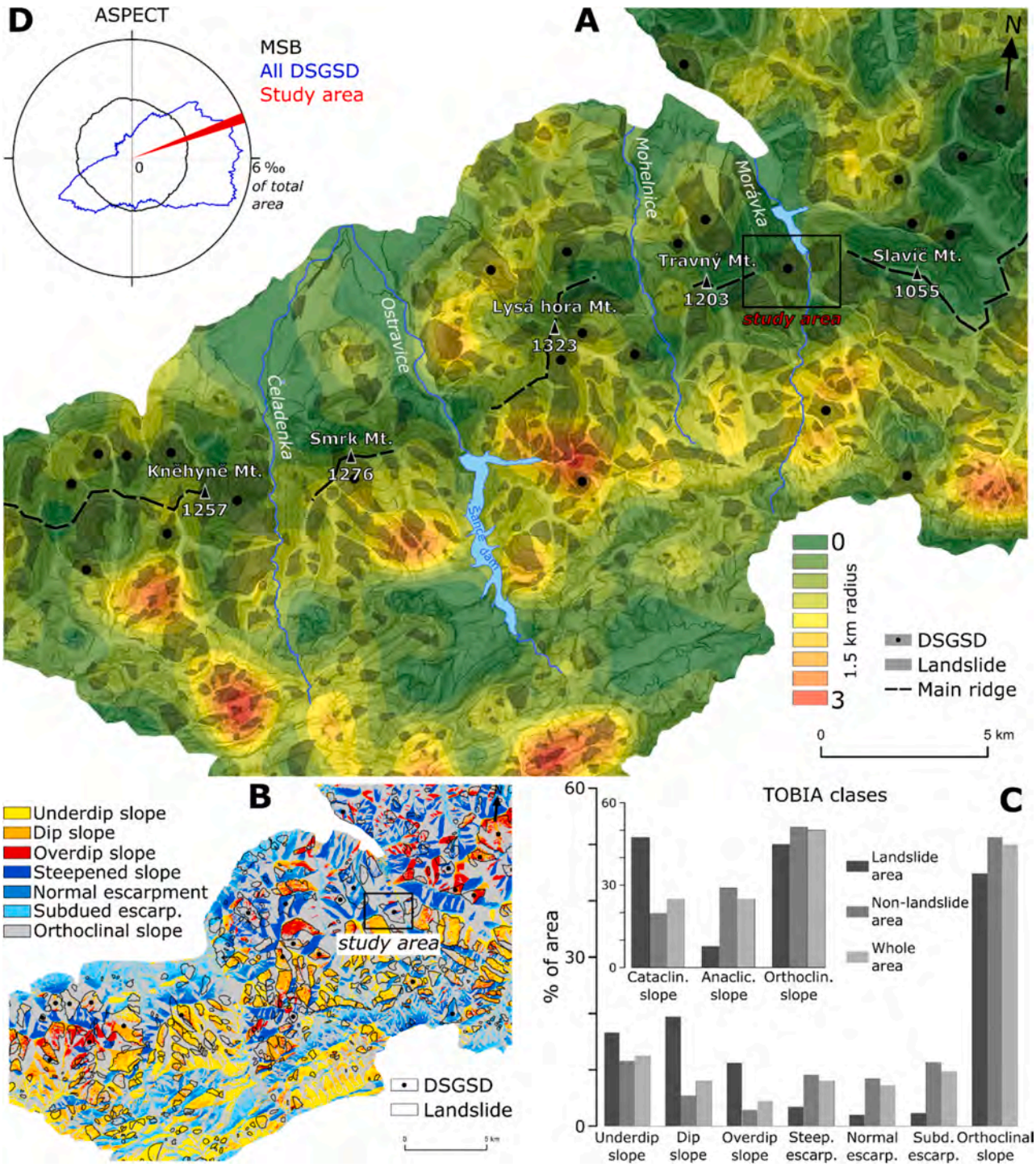

Fig. 9. A) Kernel density analysis of slope deformations within central part of MSB. B) TOBIA classification of the slopes within central part of MSB. C) TOBIA classes for the landslide, non-landslide and whole area, inserted graph shows simplified TOBIA classes. D) Distribution of slope aspect in MSB. Parts B) and C) adopted from Březný and Pánek (2017).

for investigating DSGSDs (Pánek et al., 2011). Most studies are limited to radiocarbon dating of peat bogs (Margielewski, 2006b; Chalupa et al., 2021) or cosmogenic radionuclide dating of headscarps and detached blocks (Březný et al., 2018b, 2021). The trench excavated across the antislope scarp that bounds the graben depression in the upper-northwest part of the Travný Mt. DSGSD did not reach sufficient depth to expose the deposits that record the initiation of the slope deformation at this site. Nonetheless, fluvial undermining and climatic factors seem to be the most likely triggers for the initiation of the DSGSDs in this non-glaciated and seismically quiet area (Nemčok, 1982; Margielewski, 2006b). Moreover, it seems that at some stage the associated trough was captured by a N-directed longitudinal drainage that eroded part of the sedimentary fill, leaving an incomplete stratigraphic record. Nonetheless, the exposed geometrical relationships together with the OSL ages allow constraining the two most recent displacement events occurred between 10.5 ka and 5.7 ka. The penultimate event (PE) most probably occurred at ca. 9.9 ± 0.6 ka, as indicates the OSL age obtained from the lower part of the colluvial wedge deposited soon after this surface

rupture episode. We consider this event to be a minimum age for the DSGSD. It seems that the main phases of activity of DSGSDs in OWC correspond with the major climatic changes during Late Pleistocene and Holocene. The stages with increased humidity and precipitation during the Last Glacial and with the onset of the warmer Holocene are often considered to be the possible controlling factors of mass movement activity in the OWC (Fig. 7A) (Margielewski, 2003; Starkel et al., 2013; Pánek et al., 2011, 2014; Břežný et al., 2021; Chalupa et al., 2021). The most recent event (MRE) has a poorly constrained age older than 5.7 ka, indicating that this portion of the DSGSD has been inactive for a long time. Thus, we attribute to the DSGSD an episodic kinematics. The clear geomorphic expression of the scarp can be partially attributed to erosion of deposits in the trough (hanging-wall) by the external drainage. It is likely that this information is not valid for other portions of the slope, such as Section 3, where fresh-looking scarps cross-cut older scarps. The normal fault and the joints exposed in the trench, both steeply dipping into the slope and subparallel to the slope, are consistent with the toppling of a block of competent flysch compartmentalized by joints. The outward rotation of the block and the development of a failure plane would create a keystone graben in the upper part of the slope, as support the geomorphic and geophysical evidence.

6. Conclusions

The Travný Mt. ridge in the flysch of the Czech Outer Western Carpathians displays evidence of DSGSD despite the moderate local relief and slope gradient, as well as the lack of glacial debuttresing and seismotectonic activity. Moreover, the area affected by gravitational deformations is most likely larger than that indicated by geomorphic evidence. The integration of the data gathered by multiple methods (mapping, structural analysis, geophysics, trenching) reveals that the main factors that control the development of the DSGSD are favourable litho-structural conditions and fluvial downcutting.

Faults and slope-parallel joints steeply dipping into the slope compartmentalized blocks of flysch dominated by thick-bedded sandstone that experienced outward toppling. The base of the gravitational deformation seems to be controlled by a rheological contact at the lower part of the slope between two different flysch units. Geomorphic evidence indicates that the DSGSD comprises a mosaic of different bodies with variable age.

Trenching and geochronological analyses conducted in the upper part of the main body of the DSGSD indicates that the slope movement was initiated in the late Pleistocene, has an episodic displacement regime. The two most recent events, occurred at ca. 9.9 ka and sometime before 5.7 ka, were probably associated with humid periods. This portion of the DSGSD has remained inactive during a long period, although the antislope scarp has been rejuvenated by fluvial erosion in the associated trough.

CRediT authorship contribution statement

Vladimír Chalupa: Writing – original draft, Visualization, Investigation. **Tomáš Pánek:** Writing – original draft, Investigation. **Michal Břežný:** Writing – original draft, Investigation. **Francisco Gutiérrez:** Writing – original draft, Investigation. **Alicia Medialdea:** Validation, Data curation.

Declaration of competing interest

The authors declare the following financial interests/personal relationships which may be considered as potential competing interests: Francisco Gutierrez reports financial support was provided by Spain Ministry of Science and Innovation.

Acknowledgments

The work has been supported by the projects CGL2017-85045-P and PID2021-123189NB-I00 (Spanish Government). We gratefully acknowledge Olga Chalupová, Radek Tichavský and Veronika Kapustová for assistance and valuable comments that improved the manuscript. FG belongs to the IUCA and the Geoenvironmental Processes and Global Change (E02-23R) research group financed by the Aragón Government and the European Social Fund (ESF-FSE).

Data availability

Data will be made available on request.

References

Agliardi, F., Crosta, G., Zanchi, A., 2001. Structural constraints on deep-seated slope deformation kinematics. Engineering Geology 59, 83–102. https://doi.org/10.1016/S0013-7952(00)00066-1.

Agliardi, F., Crosta, G.B., Zanchi, A., Ravazzi, C., 2009a. Onset and timing of deep-seated gravitational slope deformations in the eastern Alps, Italy. Geomorphology 103, 113–129. https://doi.org/10.1016/j.geomorph.2007.09.015.

Agliardi, F., Zanchi, A., Crosta, G.B., 2009b. Tectonic vs. gravitational morphostructures in the central Eastern Alps (Italy): constraints on the recent evolution of the mountain range. Tectonophysics 474, 250–270. https://doi.org/10.1016/j.tecto.2009.02.019.

Agliardi, F., Riva, F., Barbarano, M., Zanchetta, S., Scotti, R., Zanchi, A., 2019. Effects of tectonic structures and long-term seismicity on paraglacial giant slope deformations: Piz Dora (Switzerland). Engineering Geology 263, 105353. https://doi.org/10.1016/j.enggeo.2019.105353.

Alberto, W., Giardino, M., Martinotti, G., Tiranti, D., 2008. Geomorphological hazards related to deep dissolution phenomena in the Western Italian Alps: distribution, assessment and interaction with human activities. Eng. Geol. 99, 147–159. https://doi.org/10.1016/j.enggeo.2007.11.016.

Alexandrowicz, Z., Alexandrowicz, S.W., 1988. Ridge-top trenches and rifts in the Polish Outer Carpathians. Ann. Soc. Geol. Pol. 58, 207–228.

Alexandrowicz, S.W., Alexandrowicz, Z., 1999. Recurrent Holocene landslides: a case study of the Krynica landslide in the Polish Carpathians. The Holocene 9, 91–99. https://doi.org/10.1191/095968399674419966.

Bajgier, M., 1989. Influence of morphostructure on development of deep landslides on Skrzyczne slopes in the Beskid Śląski (Carpathians). Folia Geographica. Seria Geographica-Physica 21, 61–77.

Bovis, M.J., 1982. Uphill-facing (antislope) scarps in the Coast Mountains, Southwest British Columbia. Geol. Soc. Am. Bull. 93, 804–812.

Břežný, M., Pánek, T., 2017. Deep-seated landslides affecting monoclinal flysch morphostructure: evaluation of LiDAR-derived topography of the highest range of the Czech Carpathians. Geomorphology 285, 44–57. https://doi.org/10.1016/j.geomorph.2017.02.007.

Břežný, M., Pánek, T., Lenart, J., Grygar, R., Tábořík, P., McColl, S.T., 2018a. Sackung and enigmatic mass movement folds on a structurally-controlled mountain ridge. Geomorphology 322, 175–187. https://doi.org/10.1016/j.geomorph.2018.09.004.

Břežný, M., Pánek, T., Lenart, J., Zondervan, A., Braucher, R., 2018b. 10Be dating reveals pronounced Mid-to Late Holocene activity of deep-seated landslides in the highest part of the Czech Flysch Carpathians. Quat. Sci. Rev. 195, 180–194. https://doi.org/10.1016/j.quascirev.2018.07.030.

Břežný, M., Pánek, T., Braucher, R., Šilhán, K., Chalupa, V., Lenart, J., Tábořík, P., Team, A., 2021. Old but still active: >18 ka history of rock slope failures affecting a flysch anticline. Landslides 18, 89–104. https://doi.org/10.1007/s10346-020-01483-7.

Bunkholt, H., Redfield, T., Osmundsen, P.T., Oppikofer, T., Hermanns, R.L., Dehls, J., 2013. The role of inherited structures in deep seated slope failures in Kåfjorden, Norway. In: Margottini, C., Canuti, P., Sassa, K. (Eds.), Landslide Science and Practice. Springer Berlin Heidelberg, Berlin, Heidelberg, pp. 265–271. https://doi.org/10.1007/978-3-642-31325-7_35.

Chalupa, V., Pánek, T., Tábořík, P., Klimeš, J., Hartvich, F., Grygar, R., 2018. Deep-seated gravitational slope deformations controlled by the structure of flysch nappe outliers: insights from large-scale electrical resistivity tomography survey and LiDAR mapping. Geomorphology 321, 174–187. https://doi.org/10.1016/j.geomorph.2018.08.029.

Chalupa, V., Pánek, T., Šilhán, K., Břežný, M., Tichavský, R., Grygar, R., 2021. Low-topography deep-seated gravitational slope deformation: slope instability of flysch thrust fronts (Outer Western Carpathians). Geomorphology 389, 107833. https://doi.org/10.1016/j.geomorph.2021.107833.

Courtial-Manent, L., Mugnier, J.-L., Zerathe, S., Carcaillet, J., Vassallo, R., Ravanel, L., Tavernier, L., Buoncristiani, J.-F., 2022. Late Holocene initiation of a deep rock slope failure in an alpine valley revealed by 10Be surface exposure dating (Chamonix, France). Quat. Int. S1040618222003287. https://doi.org/10.1016/j.quaint.2022.10.001.

Crosta, G.B., Frattini, P., Agliardi, F., 2013. Deep seated gravitational slope deformations in the European Alps. Tectonophysics 605, 13–33. https://doi.org/10.1016/j.tecto.2013.04.028.

Czech Geological Survey, 2004. Bezešvá geologická mapa 1:50,000 (Seamless geological map 1:50,000). https://mapy.geology.cz/arcgis/services/Geologie/geocr50/MapServer/WMSServer (WMS server; accessed 13 October 2022).
Dabkowski, J., Frodlová, J., Hájek, M., Hájková, P., Petr, L., Fiorillo, D., Dudová, L., Horsák, M., 2019. A complete Holocene climate and environment record for the Western Carpathians (Slovakia) derived from a tufa deposit. The Holocene 29, 493–504. https://doi.org/10.1177/0959683618816443.
Delano, J.E., Gold, R.D., Briggs, R.W., Jibson, R.W., 2018. Coseismic Sackungen in the New Madrid Seismic Zone, USA. Geophys. Res. Lett. 45. https://doi.org/10.1029/2018GL080493.
Demurtas, V., Orrù, P.E., Deiana, G., 2021. Deep-seated gravitational slope deformations in central Sardinia: insights into the geomorphological evolution. J. Maps 17, 607–620. https://doi.org/10.1080/17445647.2021.1986157.
Di Luzio, E., Discenza, M.E., Di Martire, D., Putignano, M.L., Minnillo, M., Esposito, C., Scarascia Mugnozza, G., 2022. Investigation of the Luco dei Marsi DSGSD revealing the first evidence of a basal shear zone in the central Apennine belt (Italy). Geomorphology 408, 108249. https://doi.org/10.1016/j.geomorph.2022.108249.
Durcan, J., King, G., Duller, G.A.T., 2015. DRAC: Dose Rate and Age Calculator for trapped charge dating. Quat. Geochronol. 28, 54–61. https://doi.org/10.1016/j.quageo.2015.03.012.
Galbraith, R.F., Roberts, R.G., Laslett, G.M., Yoshida, H., Olley, J.M., 1999. Optical dating of single and multiple grains of quartz from Jinmium Rock Shelter, Northern Australia: part I, experimental design and statistical Models. Archaeometry 41, 339–364. https://doi.org/10.1111/j.1475-4754.1999.tb00987.x.
García-Delgado, H., 2020. The San Eduardo Landslide (Eastern Cordillera of Colombia): reactivation of a deep-seated gravitational slope deformation. Landslides 17, 1951–1964. https://doi.org/10.1007/s10346-020-01403-9.
Glueer, F., Loew, S., Manconi, A., Aaron, J., 2019. From toppling to sliding: progressive evolution of the Moosfluh Landslide, Switzerland. J. Geophys. Res. Earth Surf. 124, 2899–2919. https://doi.org/10.1029/2019JF005019.
Guérin, G., Mercier, N.G., Adamiec, G., 2011. Dose-rate conversion factors: update. Anc. TL 29, 5–8.
Guglielmi, Y., Bertrand, C., Compagnon, F., Follacci, J.P., Mudry, J., 2000. Acquisition of water chemistry in a mobile fissured basement massif: its role in the hydrogeological knowledge of the La Clapière landslide (Mercantour massif, southern Alps, France). J. Hydrol. 229, 138–148. https://doi.org/10.1016/S0022-1694(00)00166-9.
Gunnell, Y., Blondeau, S., Jarman, D., 2022. Rock slope failure in the Southern Carpathians (Romania): range-wide inventory and links with long-term mountain landscape evolution. Geomorphology 418, 108433. https://doi.org/10.1016/j.geomorph.2022.108433.
Gutiérrez, F., Ortuño, M., Lucha, P., Guerrero, J., Acosta, E., Coratza, P., Piacentini, D., Soldati, M., 2008. Late Quaternary episodic displacement on a sackung scarp in the central Spanish Pyrenees. Secondary paleoseismic evidence? Geodin. Acta 21, 187–202. https://doi.org/10.3166/ga.21.187-202.
Gutiérrez, F., Linares, R., Roque, C., Zarroca, M., Rosell, J., Galve, J.P., Carbonel, D., 2012. Investigating gravitational grabens related to lateral spreading and evaporite dissolution subsidence by means of detailed mapping, trenching, and electrical resistivity tomography (Spanish Pyrenees). Lithosphere 4, 331–353. https://doi.org/10.1130/L202.1.
Gutiérrez-Santolalla, F., Acosta, E., Ríos, S., Guerrero, J., Lucha, P., 2005. Geomorphology and geochronology of sackung features (uphill-facing scarps) in the Central Spanish Pyrenees. Geomorphology 69, 298–314. https://doi.org/10.1016/j.geomorph.2005.01.012.
Hippolyte, J.C., Bourlès, D., Braucher, R., Carcaillet, J., Léanni, L., Arnold, M., Aumaitre, G., 2009. Cosmogenic 10Be dating of a sackung and its faulted rock glaciers, in the Alps of Savoy (France). Geomorphology 108 (3-4), 312–320.
Jaboyedoff, M., Crosta, G.B., Stead, D., 2011. Slope tectonics: a short introduction. SP 351, 1–10. https://doi.org/10.1144/SP351.1.
Jaboyedoff, M., Penna, I., Pedrazzini, A., Baroň, I., Crosta, G.B., 2013. An introductory review on gravitational-deformation induced structures, fabrics and modeling. Tectonophysics 605, 1–12. https://doi.org/10.1016/j.tecto.2013.06.027.
Jarman, D., 2006. Large rock slope failures in the Highlands of Scotland: characterisation, causes and spatial distribution. Engineering Geology 83, 161–182. https://doi.org/10.1016/j.enggeo.2005.06.030.
Jarman, D., Calvet, M., Corominas, J., Delmas, M., Gunnell, Y., 2014. Large-scale rock slope failures in the eastern pyrenees: identifying a sparse but significant population in paraglacial and parafluvial contexts. Geogr. Ann. Ser. B 96, 357–391. https://doi.org/10.1111/geoa.12060.
Jomard, H., Lebourg, Th., Guglielmi, Y., 2014. Morphological analysis of deep-seated gravitational slope deformation (DSGSD) in the western part of the Argentera massif. A morpho-tectonic control? Landslides 11, 107–117. https://doi.org/10.1007/s10346-013-0434-0.
Kasprzak, M., Duszyński, F., Jancewicz, K., Michniewicz, A., Różycka, M., Migoń, P., 2016. The Rogowiec Landslide Complex (Central Sudetes, SW Poland) – a case of a collapsed mountain. GQ. https://doi.org/10.7306/gq.1286.
Kasprzak, M., Jancewicz, K., Różycka, M., Kotwicka, W., Migoń, P., 2019. Geomorphology- and geophysics-based recognition of stages of deep-seated slope deformation (Sudetes, SW Poland). Engineering Geology 260, 105230. https://doi.org/10.1016/j.enggeo.2019.105230.
Kłapyta, P., 2020. Geomorphology of the high-elevated flysch range – Mt. Babia Góra Massif (Western Carpathians). J. Maps 16, 689–701. https://doi.org/10.1080/17445647.2020.1800530.
Komura, K., Kaneda, H., Tanaka, T., Kojima, S., Inoue, T., Nishio, T., 2020. Synchronized gravitational slope deformation and active faulting: a case study on and around the Neodani fault, central Japan. Geomorphology 365, 107214. https://doi.org/10.1016/j.geomorph.2020.107214.
Łajczak, A., 2014. Relief development of the Babia Góra massif, Western Csrpathian Mountains. Quaestiones Geographicae 33, 89–106. https://doi.org/10.2478/quageo-2014-0006.
Łajczak, A., Czajka, B., Kaczka, R.J., 2014. The new features of landslide relief discovered using Lidar – case study from Babia Góra Massif, Western Carpathian Mountains. Quaestiones Geographicae 33, 77–88. https://doi.org/10.2478/quageo-2014-0031.
Lebourg, T., Zerathe, S., Fabre, R., Giuliano, J., Vidal, M., 2014. A Late Holocene deep-seated landslide in the northern French Pyrenees. Geomorphology 208, 1–10. https://doi.org/10.1016/j.geomorph.2013.11.008.
Lenart, J., Kašing, M., Táborík, P., Piotrowska, N., Pawlyta, J., 2018. The Cirilka Cave–the longest crevice-type cave in Czechia: structural control, genesis and age. Int. J. Speleol. 47, 379–392.
Livio, F.A., Zerboni, A., Ferrario, M.F., Mariani, G.S., Martinelli, E., Amit, R., 2022. Triggering processes of deep-seated gravitational slope deformation (DSGSD) in an un-glaciated area of the Cavargna Valley (Central Southern Alps) during the Middle Holocene. Landslides 19, 1825–1841. https://doi.org/10.1007/s10346-022-01892-w.
Lo Russo, S., Forno, M.G., Taddia, G., Gnavi, L., 2012. Predisposing Factors and Susceptibility Assessment for Deep-seated Gravitational Slope Deformations (DSGSDs): A Case Study (NW Alps, Italy), 8286.
Loke, M.H., 1997. Electrical Imaging Surveys for Environmental and Engineering Studies. A Practical Guide to 2-D and 3-D Surveys. Geotomo software. http://www.geotomosoft.com (accessed 20 October 2022).
Loke, M.H., Barker, R.D., 1996. Rapid least-squares inversion of apparent resistivity 455 pseudosections by a quasi-Newton method. Geophys. Prospect. 44, 131–152.
Margielewski, W., 2003. Late glacial-Holocene palaeoenvironmental changes in the Western Carpathians: case studies of landslide forms and deposits. Folia Quaternaria 74.
Margielewski, W., 2006a. Structural control and types of movements of rock mass in anisotropic rocks: case studies in the Polish Flysch Carpathians. Geomorphology 77, 47–68. https://doi.org/10.1016/j.geomorph.2006.01.003.
Margielewski, W., 2006b. Records of the Late glacial - Holocene palaeoenvironmental changes in landslide forms and deposits of the Beskid Makowski and Beskid Wyspowy Mts. area (Polish outer Carpathians). Folia Quaternaria 76.
Margielewski, W., Krąpiec, M., Valde-Nowak, P., Zernitskaya, V., 2010. A Neolithic yew bow in the Polish Carpathians. Catena 80, 141–153.
Margielewski, W., Kolaczek, P., Michczynski, A., Obidowicz, A., Pazdur, A., 2011. Record of the Meso- and Neoholocene palaeoenvironemntal changes in the Jesionowa landslide peat bog (Beskid Sadecki MTS. Polish Outer Carpathians). Geochronometria 38, 138–154.
McCalpin, J.P., 2009. Paleoseismology, 2nd edition. Academic Press, Amsterdam-London. 615 p.
McCalpin, J.P., Corominas, J., 2019. Postglacial deformation history of sackungen on the northern slope of Pic d'Encampadana, Andorra. Geomorphology 337, 134–150. https://doi.org/10.1016/j.geomorph.2019.04.007.
McCalpin, J.P., Jones, L.C., 2021. The Stillwater Scarp, Central Nevada, USA; coseismic gravitational failure on a 1.200-M-high range-front escarpment. Environ. Eng. Geosci. 27 (4), 377–393.
McCalpin, J.P., Liščík, P., Jelínek, R., Zorba, M.O., Santacana, N., 2019. Postglacial deformation history of sackungen on the southerns slope of Mount Chabanec, Nízké tatry Mts., Slovakia. Mineralia Slovaca 51, 1–30.
McGill, G.E., Stromquist, A.W., 1979. The grabens of Canyonlands National Park, Utah: geometry, mechanics, and kinematics. J. Geophys. Res. 84, 4547. https://doi.org/10.1029/JB084iB09p04547.
Menčík, E., 1989. Základní geologická mapa 1:25,000, 25–224 Morávka (Basic geological map 1:25,000, 25–224 Morávka). Ústř. Úst. Geol, Brno (in Czech).
Menčík, E., Tyráček, J., 1985. Přehledná geologická mapa Beskyd a Podbeskydské pahorkatiny v měřítku 1:100,000 (Overview geological map of Beskydy Mts. and Podbeskydská pahorkatina Upland, 1:100,000). Ústř. Úst. Geol., Praha (in Czech).
Menčík, E., Adamová, M., Dvořák, J., Dudek, A., Jetel, J., Jurková, A., Hanzlíková, E., Houša, V., Peslová, H., Rybářová, L., Šmíd, B., Šebesta, J., Tyráček, J., Vašíček, Z., 1983. Geologie Moravskoslezských Beskyd a Podbeskydské pahoraktiny (Geology of Moravskoslezské Beskydy Mts. and Podbeskydská pahorkatina Upland). Ústř. Úst. Geol., Praha (in Czech).
Moreno, D., Gutiérrez, F., del val, M., Carbonel, D., Jiménez, F., Alonso, M.J., Martínez-Pillado, V., Guzmán, O., López, G.I., Martínez, D., 2021. A multi-method dating approach to reassess the geochronology of faulted Quaternary deposits in the central sector of the Iberian Chain (NE Spain). Quat. Geochronol. 65, 101185.
Nemčok, A., 1982. Zosuvy v slovenských Karpatoch (Landslides in the Slovak Carpathians). Publ. VEDA, Bratislava (in Slovak).
Novosad, S., 1966. Porušení svahů v godulských vrstvách Moravskoslezských Beskyd (Slope disturbances in the Godula Group of the Moravskoslezské Beskydy Mountains). Sbor. Geol, Věd (in Czech).
Pánek, T., Táborík, P., Klimeš, J., Komárková, V., Hradecký, J., Šťastný, M., 2011. Deep-seated gravitational slope deformations in the highest parts of the Czech Flysch Carpathians: evolutionary model based on kinematic analysis, electrical imaging and trenching. Geomorphology 129, 92–112. https://doi.org/10.1016/j.geomorph.2011.01.016.
Pánek, T., Smolková, V., Hradecký, J., Baroň, I., Šilhán, K., 2013. Holocene reactivations of catastrophic complex flow-like landslides in the Flysch Carpathians (Czech Republic/Slovakia). Quatern. Res. 80, 33–46. https://doi.org/10.1016/j.yqres.2013.03.009.
Pánek, T., Hartvich, F., Jankovská, V., Klimeš, J., Táborík, P., Bubík, M., Smolková, V., Hradecký, J., 2014. Large Late Pleistocene landslides from the marginal slope of the

Flysch Carpathians. Landslides 11, 981–992. https://doi.org/10.1007/s10346-013-0463-8.
Pánek, T., Mentlík, P., Engel, Z., Braucher, R., Zondervan, A., 2017. Late Quaternary sackungen in the highest mountains of the Carpathians. Quaternary Science Reviews 159, 47–62. https://doi.org/10.1016/j.quascirev.2017.01.008.
Pánek, T., Březný, M., Kapustová, V., Lenart, J., Chalupa, V., 2019. Large landslides and deep-seated gravitational slope deformations in the Czech Flysch Carpathians: new LiDAR-based inventory. Geomorphology 346, 106852. https://doi.org/10.1016/j.geomorph.2019.106852.
Pasquarè Mariotto, F., Tibaldi, A., 2016. Inversion kinematics at deep-seated gravity slope deformations: a paleoseismological perspective (preprint). In: Landslides and Debris Flows Hazards. https://doi.org/10.5194/nhessd-3-4585-2015.
Prescott, J.R., Hutton, J.T., 1994. Cosmic ray contributions to dose rates for luminescence and ESR dating: large depths and long term time variations. Radiat. Meas. 23, 497–500. https://doi.org/10.1016/1350-4487(94)90086-8.
Reimer, P.J., Bard, E., Bayliss, A., Beck, J.W., Blackwell, P.G., Bronk Ramsey, C., Grootes, P.M., Guilderson, T.P., Haflidason, H., Hajdas, I., Hattz, C., Heaton, T.J., Hoffmann, D.L., Hogg, A.G., Hughen, K.A., Kaiser, K.F., Kromer, B., Manning, S.W., Niu, M., Reimer, R.W., Richards, D.A., Scott, E.M., Southon, J.R., Staff, R.A., Turney, C.S.M., van der Plicht, J., 2013. IntCal13 and Marine13 radiocarbon age calibration curves 0-50,000 years cal BP. Radiocarbon 55, 1869–1887.
Sandmeier software, 2019. REFLEXW. Sandmeier Geophysical Research.
Starkel, L., Michczyńska, D., Krąpiec, M., Margielewski, W., Nalepka, D., Pazdur, A., 2013. Progress in the holocene chrono-climatostratigraphy of Polish territory. Geochronometria 40, 1–21. https://doi.org/10.2478/s13386-012-0024-2.
State Administration of Land Surveying and Cadastre, 2017. Digital Elevation Model of Czech Republic, 5th Generation (DEM 5G).
Szalai, S., Szarka, L., 2008. Parameter sensitivity maps of surface geoeletric arrays. Part 1: linear arrays. Acta Geod. Geophys. Hung. 43, 419–437.
Szalai, S., Novák, A., Szarka, L., 2009. Depth of investigation and vertical resolution of surface geoelectric arrays. J. Environ. Eng. Geophys. 14, 15–23.
Teshebaeva, K., Echtler, H., Bookhagen, B., Strecker, M., 2019. Deep-seated gravitational slope deformation (DSGSD) and slow-moving landslides in the southern Tien Shan Mountains: new insights from InSAR, tectonic and geomorphic analysis. Earth Surf. Process. Landforms 44, 2333–2348. https://doi.org/10.1002/esp.4648.
Vick, L.M., Böhme, M., Rouyet, L., Bergh, S.G., Corner, G.D., Lauknes, T.R., 2020. Structurally controlled rock slope deformation in northern Norway. Landslides 17, 1745–1776. https://doi.org/10.1007/s10346-020-01421-7.
Wagner, J., Demek, J., Stráník, Z., 1990. Jeskyně Moravskoslezských Beskyd a okolí (Caves of the Moravskoslezské Beskydy Mountains and Their Surrounding). Knihovna České speleologické společnosti, Praha (in Czech).
Zhou, W., Beck, B.F., Adams, A.L., 2002. Effective electrode array in mapping karst hazards in electrical resistivity tomography. Environ. Geol. 42, 922–928.